

Quantum anomalous Hall effect in two dimensional Janus $\text{Mn}_2\text{Cl}_3\text{Br}_3$ with large magnetic anisotropy energy

Ping Li¹ and Tian-Yi Cai^{1,*}

¹*School of Physical Science and Technology, Soochow University, Suzhou 215006, People's Republic of China*
(Dated: December 21, 2024)

The quantum anomalous Hall (QAH) effect have been experimentally observed in magnetically-doped topological insulators. However, the QAH effect only at extremely low temperatures due to the weak magnetic coupling, small band gap and low carrier mobility. Here, based on first-principles density functional theory, we predict that the Janus $\text{Mn}_2\text{Cl}_3\text{Br}_3$ is high Curie temperature ferromagnet that host the QAH phase. Furthermore, we find that it is a Dirac half-metal characterized by a Dirac cone in one spin channel with carrier mobilities comparable to freestanding germanene and an large band gap in other spin channel. Simultaneously, when the spin-orbital coupling interaction is considered, the Janus $\text{Mn}_2\text{Cl}_3\text{Br}_3$ exhibit lager magnetic anisotropic energy of 11.89 meV/cell and a nontrivial band gap. More interestingly, both the Chern number sign and the chiral edge current are tuned by changing the direction of magnetization. Our finding would suggest the possibility of not only realized the QAH effect but also designed the flow direction of the edge current.

I. INTRODUCTION

The quantum Hall (QH) effect is novel quantum topological state that is realized in the absence of time reversal symmetry (TRS). [1] The TRS is broken by an external magnetic field and its topological origin is uncovered by the quantized Hall conductance. [2] However, an external magnetic field is not necessary for the new QH state which is firstly proposed by Haldane. [3] The new QH effect realized in the absence of a magnetic field is called quantum anomalous Hall (QAH) effect. The QAH state is characterized by chiral edge states that encloses an insulating bulk. [4]. The dissipationless unidirectional electrical current without the need for an external magnetic field provides fascinating applications in low energy consumption electronics and spintronics. [5]

Up to now, the enormous Chern insulator have been theoretically predicted, including $\text{Hg}_{1-y}\text{Mn}_y\text{Te}$ quantum wells, [6] magnetically-doped $(\text{Bi,Sb})_2\text{Te}_3$ thin films, [7] graphene, [8–11] silicene, [12–15] germanene, [16] stanene, [16, 17] transition metal oxides, [18–20] metal organic frameworks, [21–23] transition metal halides, [24–27] and other. [28] Among these, only the V or Cr doped $(\text{Bi,Sb})_2\text{Te}_3$ systems have been experimentally realized the QAH effect. [29–31] Unfortunately, all the experimentally observed the QAH effect are achieved at the extremely low temperature (30 mK). It is a daunting challenge for device applications. Obviously, it would be meaningful to search for a large band gap and high Curie temperature (T_C) Chern insulator.

In this work, we predict that the high-temperature QAH effect can be realized in two-dimensional (2D) Janus $\text{Mn}_2\text{Cl}_3\text{Br}_3$. We find that the magnetic anisotropy energy reach up 11.89 meV/cell. Furthermore, spin-polarized band structure calculation show Dirac half-metal. The spin up bands is metallic with Dirac cone at

the high symmetry K point near the Fermi level, while spin down bands is insulating with a gap of 4.09 eV. Moreover, the non-trivial band gap is opened by spin-orbital coupling (SOC). The QAH effect is clearly confirmed by the calculated Chern number $C = 1$ and chiral edge states. More interestingly, the chiral edge currents and the sign of Chern number can be tunable by changing the direction of magnetization. Recently, the successful synthesized 2D Janus MoSSe [32, 33] pave the way for verifying QAH effect in $\text{Mn}_2\text{Cl}_3\text{Br}_3$. These results offer a platform for investigating high-temperature QAH effect and potential applications in spintronics.

II. STRUCTURES AND COMPUTATIONAL METHODS

To investigate the electronic and magnetic structures, we implemented the Vienna *Ab initio* Simulation Package (VASP) [34, 35] for the first-principles calculations based on density functional theory (DFT). The electron exchange-correlation functional was described by the generalized gradient approximation of the Perdew-Burke-Ernzerhof functional. [36] The plane-wave basis set with a kinetic energy cutoff of 500 eV was employed. Here, $12 \times 12 \times 1$ and $24 \times 24 \times 1$ Γ -centered k meshes are adopted for the structural optimization and the self-consistent calculations. To avoid unnecessary interactions between the monolayer, the vacuum layer was set to 20 Å. The total energy convergence criterion was set to be 10^{-6} eV. What's more, to describe the strongly correlated 3d electrons of the Mn atom, the GGA + U method was used. [37] The onsite Coulomb repulsion U of Mn atom is set to 4 eV. [38, 39] To confirm the structural stability, the phonon spectra were calculated using a finite displacement approach as implemented in the PHONOPY code, in which a $4 \times 4 \times 1$ supercell were used. [40] An effective tight-binding Hamiltonian constructed from the maximally localized Wannier functions

* caitianyi@suda.edu.cn

(MLWFs) was employed to explore the edge states. [41–43] Therefore, the edge states were calculated in a half-infinite boundary condition using the iterative Green’s function method by the package WannierTools. [43, 44]

III. RESULTS AND DISCUSSION

A. Structure and stability

As shown in Figure 1 (a), monolayer Janus $\text{Mn}_2\text{Cl}_3\text{Br}_3$ have a layered hexagonal structure. It can be seen that Janus $\text{Mn}_2\text{Cl}_3\text{Br}_3$ consists of three flat atomic layers, composing of hexagonal Mn layer sandwiched between the Cl and Br layers with unequal distance. $\text{Mn}_2\text{Cl}_3\text{Br}_3$ inversion symmetry have broken while it shows mirror asymmetry with relating to the Mn atomic layer. Each of the Mn atoms are surrounded by six first-nearest-neighbor Cl and Br atoms in an octahedral environment. The lattice constant is calculated to be 6.46 Å, and Mn-Cl and Mn-Br bond lengths are 2.43 Å and 2.64 Å, respectively.

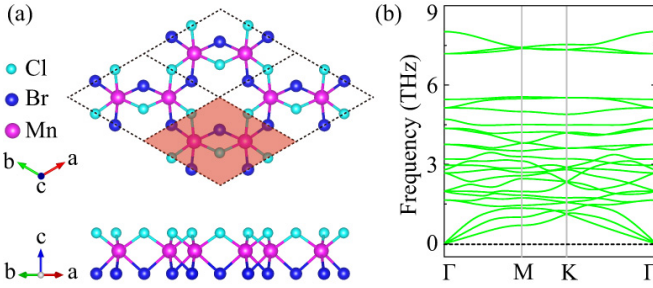


FIG. 1. (a) Top and side view of the lattice structure for $\text{Mn}_2\text{Cl}_3\text{Br}_3$ monolayer, the unit cell is indicated by the magenta shading. The Cl, Br and Mn atoms are depicted by the light blue, dark blue and magenta balls, respectively. (b) The calculated phonon dispersion curves.

To characterize the thermodynamic stability of the Janus $\text{Mn}_2\text{Cl}_3\text{Br}_3$, we define the cohesive energy E_c as $E_c = (\sum N_i \mu_i - E_{tot})/N$. Here, μ_i is the chemical potential of i atom which is chosen to be the total energy of an isolated i atom. E_{tot} is the total energies of Janus $\text{Mn}_2\text{Cl}_3\text{Br}_3$. $N = \sum N_i \mu_i$, N_i and N and the number of i atom and all atoms in the primitive unit cell, respectively. The cohesive energy is 2.66 eV/atom, which larger than Janus MoSSe (0.78 eV/atom). [45] The Janus MoSSe have recently been experimentally synthesized, [32, 33] also indicating that Janus $\text{Mn}_2\text{Cl}_3\text{Br}_3$ could be synthesized experimentally. Furthermore, the dynamic stability of $\text{Mn}_2\text{Cl}_3\text{Br}_3$ is confirmed by its phonon spectrum without negative frequencies of the vibrational modes, as shown in Figure 1 (d).

B. The Curie temperature and magnetic anisotropy energy

The transition metal elements usually carry magnetic moments because of their partially filled d shell. The materials including Mn atom hence usually exhibit magnetic interactions, which is the case for Janus $\text{Mn}_2\text{Cl}_3\text{Br}_3$. As shown in Figure 2 (a), we consider all possible magnetic configurations in the 2×2 supercell, namely, the ferromagnetic (FM), antiferromagnetic-Neel (AFM-N), antiferromagnetic-stripy (AFM-ST), antiferromagnetic-zigzag (AFM-ZZ), antiferromagnetic-cluster-I (AFM-C-I), antiferromagnetic-cluster-II (AFM-C-II), and antiferromagnetic-cluster-III (AFM-C-III). Nonetheless, we find that the initial AFM-ST magnetic configuration always converges to the nonmagnetic state. It reveal that the metastable AFM-ST magnetic configuration does not exist in the system. As Table I shows, the FM state has the lowest total energy. Therefore, the FM state is the ground state and has an integer magnetic moment of $8 \mu_B$ per unit cell. This amounts to the $d^{4\uparrow 0\downarrow}$ spin configuration of Mn^{3+} , which can be verified by the Bader charge analysis. [46]

TABLE I. Different magnetic configuration of the total energy E (meV/cell) (relative to the FM state), total spin magnetic moment m^t (μ_B /cell) and spin magnetic moments of Mn atom m^{Mn} (μ_B /cell).

	FM	AFM-N	AFM-ZZ	AFM-C-I	AFM-C-II	AFM-C-III
E	0.00	562.99	257.06	446.08	389.98	397.44
m^t	32.00	0.00	0.00	0.00	0.00	0.00
m^{Mn}	4.34	4.29	4.33	4.32	4.32	4.33

To further understand the origin of magnetic moments, we analyse the crystal symmetry of Mn-3d orbitals. As illustrated in Figure 3, the Mn-3d orbitals are split into two e_g and three t_{2g} orbitals in a perfect octahedral crystal field. Due to the structural asymmetry, structural distortion of the $\text{Mn}_2\text{Cl}_3\text{Br}_3$ octahedron makes the t_{2g} orbitals further split into the double generated e and one a orbitals. The e orbital is energetically higher than a orbital. When consider an exchange field by magnetic interaction, the degenerate e , a , and e_g orbitals split because of Hund’s rule. Therefore, for the Mn^{3+} state, four electrons with only spin up channel fully occupy the d_{z^2} , d_{xy} , and $d_{x^2-y^2}$ orbitals, while only one electron occupy the degenerate d_{xz} and d_{yz} orbitals. So, the magnetic moment is an integer $8 \mu_B$ in per unit cell. The result is consistent the Bader charge analysis.

To fully demonstrate both kinds of analysis, we calculate the partial density of states (PDOS) of d states for one Mn atom, as shown in Figure 4. From seeing the PDOS, the spin up channel of d_{z^2} , d_{xy} , and $d_{x^2-y^2}$ orbitals are fully occupied, while the spin up channel of d_{xz} and d_{yz} are partially occupied around the Fermi level. It is in agreement both kinds of analysis, so the Mn^{3+} spin configuration is $d^{4\uparrow 0\downarrow}$.

The Mermin-Wagner theorem point out that the long-

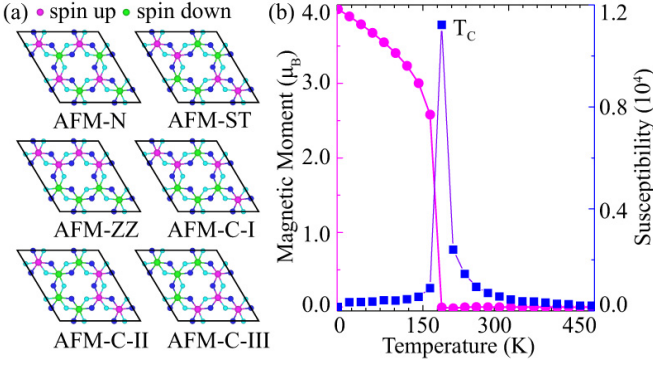


FIG. 2. (a) Top view of various AFM spin configurations: AFM-Neel (AFM-N), AFM-stripy (AFM-ST), AFM-zigzag (AFM-ZZ), AFM-cluster-I (AFM-C-I), AFM-cluster-II (AFM-C-II) and AFM-cluster-III (AFM-C-III), where the blue (green) circles denote the up (down) spins. (b) Monte Carlo simulations the average magnetic moment (magenta) and spin susceptibility (blue) per unit cell with respect to the temperature calculated for $\text{Mn}_2\text{Cl}_3\text{Br}_3$.

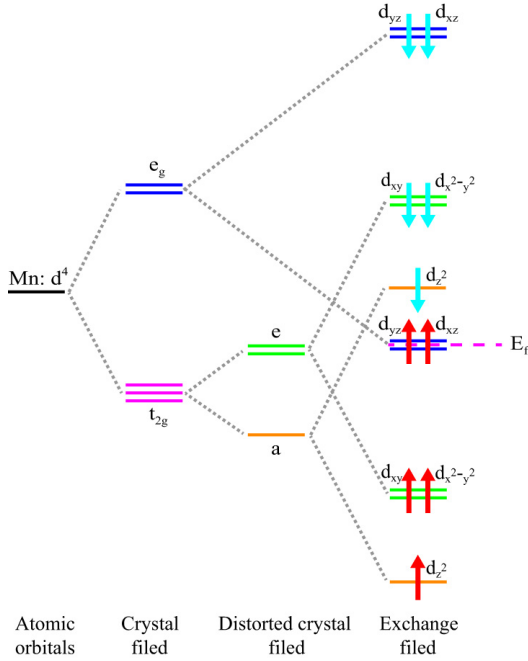


FIG. 3. Energy level diagram of Mn^{3+} in $\text{Mn}_2\text{Cl}_3\text{Br}_3$.

range magnetic has been notably absent by thermal fluctuations in 2D material. [47] However, there are two models that can exhibit magnetic ordering in 2D material: the 2D XY model and Ising model. In the XY model, the spins show a preferred plane in the magnetic system. In this case, the material display a quasi-long-range ordered phase at low temperature. The magnetization show an easy axis in the Ising model. For this case, the material display a second order phase transition to a magnetically ordered phase. Hence, where the 2D

material show a magnetically ordered phase rely on the magnetic anisotropy energy (MAE).

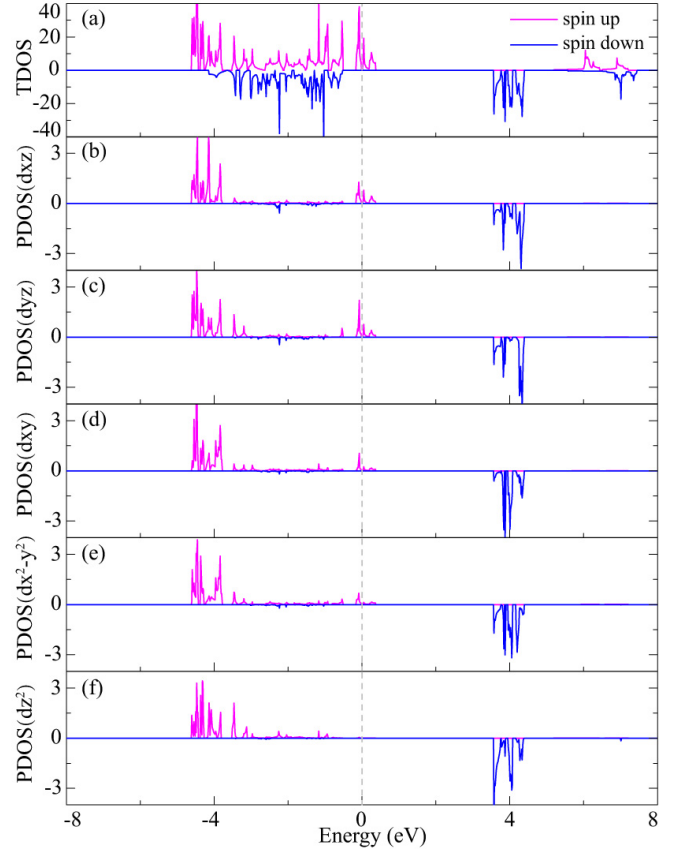


FIG. 4. (a) Calculated total density of states for $\text{Mn}_2\text{Cl}_3\text{Br}_3$. (b-f) The partial density of states (PDOS) of d states for one Mn atom are shown.

Here, we consider two magnetization directions, namely, the in plane ([100] direction) and out of plane ([001] direction). The SOC are included in all the energy calculations. The MAE defined as $\Delta E = E_{100} - E_{001}$. The positive value of MAE shows the easy axis is along the z axis rather than along the x axis. The MAE is 11.89 meV/cell, indicating the magnetization along the z axis. Moreover, this also implies that $\text{Mn}_2\text{Cl}_3\text{Br}_3$ belongs to the category of XY magnet. It is eight times more than that of 2D CrI_3 (1.37 meV/cell). [48] More interestingly, the experiment reported that the magnetization direction of 2D ferromagnets could be tuned by an external field in Fe_3GeTe_2 system. [49]

Based on the octahedral symmetry of Janus $\text{Mn}_2\text{Cl}_3\text{Br}_3$, the angular dependence of the MAE can be described using the equation:

$$MAE = K_1 \cos^2 \theta + K_2 \cos^4 \theta, \quad (1)$$

where K_1 (42.90 meV) and K_2 (-31.01 meV) are the MAE constant and θ is the azimuthal angle of rotation. As shown in Figure 5, the MAE of Janus $\text{Mn}_2\text{Cl}_3\text{Br}_3$ in the xz plane can be fitted very well by this equation. The

MAE show a strong dependence on the xz plane, while exhibit a weak dependence on the xy plane. It confirm again the strong magnetic anisotropy in the system.

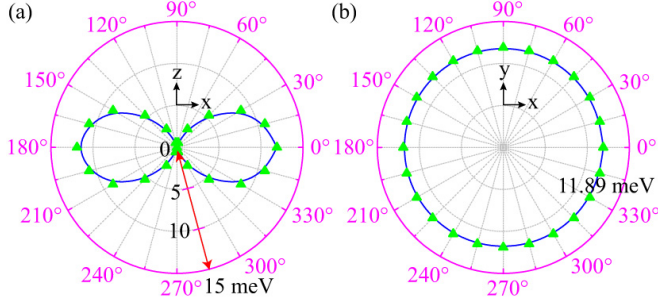


FIG. 5. Angular dependence of the magnetic anisotropy energy (MAE) of $\text{Mn}_2\text{Cl}_3\text{Br}_3$ with the direction of magnetization lying on different planes (a) on the xz plane and (b) on the xy plane.

As is well-known, the Curie temperature (T_C) of the ferromagnetic material positively correlates with its MAE. The large MAE indicates that high T_C can be anticipated in Janus $\text{Mn}_2\text{Cl}_3\text{Br}_3$. Hence, based on the Heisenberg model, we estimate the Curie temperature by using Monte Carlo (MC) simulations. The nearest neighbor exchange interaction parameters J can be described by the Hamiltonian of the Heisenberg model:

$$H = - \sum_{i,j} JS_i \cdot S_j - AS_{iz}^2, \quad (2)$$

where S is the spin magnetic moment per Mn atom, i and j stand for the nearest site pairs. A is the anisotropy parameter. The exchange interaction parameter J is defined from the exchange energy as $J = E_{ex}/6S^2$, where $E_{ex} = (E_{AFM} - E_{FM})$ is the energy difference between the AFM-N and FM state. Therefore, the exchange interaction parameter J can be obtained to be 5.87 meV. Here, the MC simulations are implemented on a 80×80 supercell which is adopted to reduce translational constraint, using 1×10^7 loops for each temperature. As shown in Figure 2(b), the simulated magnetic moment and spin susceptibility of $\text{Mn}_2\text{Cl}_3\text{Br}_3$ with respect to temperature show that the T_C of $\text{Mn}_2\text{Cl}_3\text{Br}_3$ is 183 K. It is significantly higher than CrI_3 (45 K). [50]

C. Electronic band structure

We next investigate the electronic band structure. The spin-polarized band structure is displayed in Figure 6. Figure 6(a) and (b) show the spin up and spin down bands, respectively. Remarkably, the Janus $\text{Mn}_2\text{Cl}_3\text{Br}_3$ is 100 % spin-polarized Dirac half-metal. The spin up bands are metallic with Dirac cone at the high symmetry K point near the Fermi level, while spin down bands are insulating with a gap of 4.09 eV. Furthermore, the Fermi

velocity is acquired from the linear-like energy dispersion, with value of $(\partial\varepsilon/\partial k)\hbar^{-1} = 3.79 \times 10^5$. [51] It is close to the value of 5.50×10^5 in freestanding germanene. [52] The combination of massless Dirac fermion and 100 % spin-polarized electron render a candidate for future application in optoelectronics and spintronics.

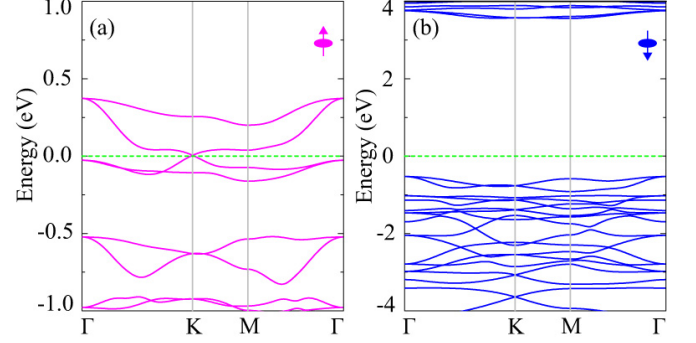


FIG. 6. Spin-polarized band structure for $\text{Mn}_2\text{Cl}_3\text{Br}_3$, (a) spin up bands and (b) spin down bands.

To understand the origin of Dirac states in the Janus $\text{Mn}_2\text{Cl}_3\text{Br}_3$, we make the orbital resolved of spin up band structures, as shown in Figure 7. One can see that the Dirac states are mainly contributed by the Br p_x and p_y orbitals. The $p_{x,y}$ Dirac states are particularly robust due to the nature of strong σ bonds. [15] The feature is different from the p_z Dirac states because of the nature of weak π bonds. [53]

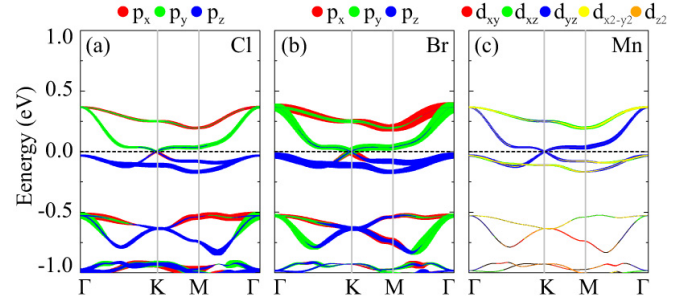


FIG. 7. Energy and k contribution of Cl-p (a), Br-p (b) and Mn-d (c) resolved to the spin up bands.

We know that the easy magnetization axis is z axis from the MAE analysis. Hence, when the SOC interaction is considered, we firstly calculate the magnetization direction along z axis of band structure, as shown in Figure 8(c). The band gap opens to 28.38 meV. When the magnetization direction are tuned to the x axis, the band gap enlarge to 32.49 meV, as show in Figure 8(a). From the above results, we know that the Dirac cone open the band gap whether the magnetization direction along z or x axis, considering the SOC effect. These pave the way for the topological properties of the Janus $\text{Mn}_2\text{Cl}_3\text{Br}_3$.

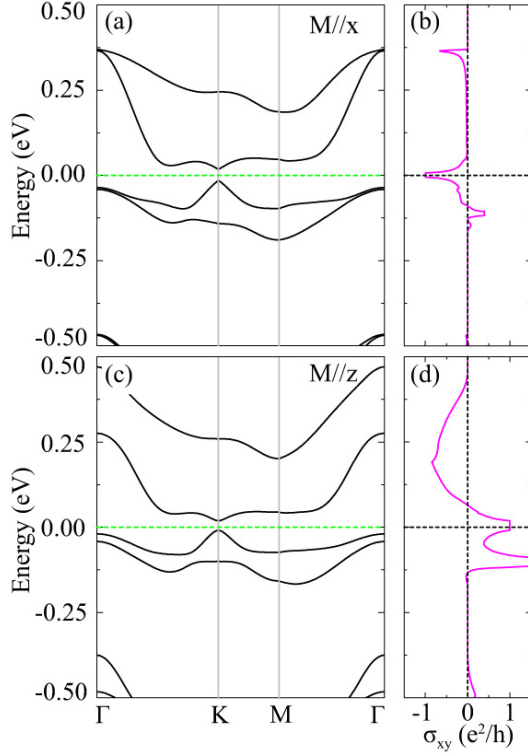


FIG. 8. Band structures with SOC as well as anomalous Hall conductivity (σ_{xy}) of the magnetization along the x-axis (a, b) and the magnetization along the z-axis (c, d).

D. Quantum anomalous Hall effect

To ensure the topological properties of Janus $\text{Mn}_2\text{Cl}_3\text{Br}_3$, we calculate the anomalous Hall conductivity (AHC) by using the formula

$$\sigma_{xy} = C \frac{e^2}{h}, \quad (3)$$

$$C = \frac{1}{2\pi} \int_{BZ} d^2k \Omega(\mathbf{k}), \quad (4)$$

where C is related to the anomalous Hall conductance σ_{xy} , namely, Chern number. [54] The right panel of Figure 8 shows the σ_{xy} relative to the Fermi level. The σ_{xy} shows a quantized value with $C = 1$ when the magnetization direction along z axis, confirming the Chern insulator. More interestingly, when the magnetization direction tuned to x axis, Chern number change $C = -1$. It implies that the direction of the chiral edge current can be tuned by the changed magnetization direction.

In addition,

$$\Omega(\mathbf{k}) = - \sum_n f_n \sum_{n' \neq n} \frac{2Im \langle \psi_{nk} | v_x | \psi_{n'k} \rangle \langle \psi_{n'k} | v_y | \psi_{nk} \rangle}{(E_{n'} - E_n)^2}, \quad (5)$$

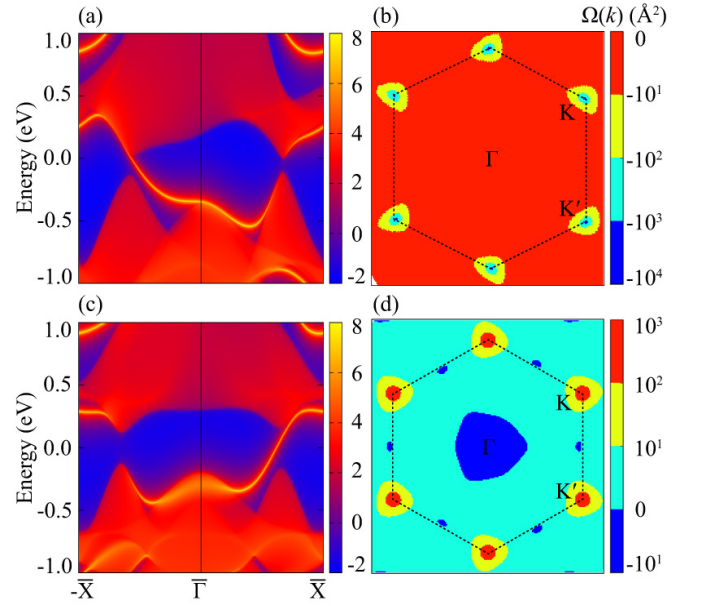


FIG. 9. Calculated edge state of a semi-infinite sheet and the Berry curvature with SOC of the magnetization along the x-axis (a, b) and the magnetization along the z-axis (c, d).

where $\Omega(\mathbf{k})$ is the Berry curvature in the reciprocal space, v_x and v_y are operator components along the x and y directions and $f_n = 1$ for the occupied bands. [55] The Berry curvature in the Brillouin zone are displayed in Figure 9(b) and (d), the Berry curvature mainly shows around the K and K' points, which offer an QAH effect. The Berry curvature have the opposite sign when the magnetization direction along x and z axis. It is consistent with the opposite Chern value when the magnetization direction along x and z axis

Another prominent characteristic of Chern insulator is the existence of chiral edge states. Therefore, in order to further examine the topological properties, we constructed the Green's function of the $\text{Mn}_2\text{Cl}_3\text{Br}_3$ semi-infinite sheet from the MLWFs and calculated the local density of states at the edge, as shown in Figure 9(a) and (c). [56, 57] We can clearly see that one chiral edge state connects the valence and conduction bands. The direction of the chair edge current is opposite when the magnetization direction along x and z axis. Moreover, the number of edge states indicates the absolute value of the Chern number, which is $|C| = 1$. [58] What's more, the calculated FM ordering temperature as high as 183 K for Janus $\text{Mn}_2\text{Cl}_3\text{Br}_3$. However, the band gap of $28.38 \sim 32.49$ meV correspond to $331 \sim 379$ K. The temperature is large enough to retain the FM state. The conclusion is that the Janus $\text{Mn}_2\text{Cl}_3\text{Br}_3$ provide a promising platform for investigating the QAH effect at 183 K, which is three orders of magnitude higher than the temperature of 30 mK at which the QAH effect was recently observed in Cr-doped Bi_2Se_3 films. [29] Therefore, the Janus structure can be provided a QAH insulator.

IV. CONCLUSION

In summary, we predict that the Janus $\text{Mn}_2\text{Cl}_3\text{Br}_3$ is Dirac half-metal which shows many intriguing properties, such as 100 % spin polarization, large magnetic moment, large magnetic anisotropy energy, high Curie temperature, and massless Dirac fermion with high carrier mobility. When the spin-orbit coupling is considered, the Dirac cone opens the nontrivial topological band gap. Remarkably, in the quantum anomalous Hall state both the chiral edge currents and the sign of Chern number can be tuned by changing the direction of magnetiza-

tion. Our work demonstrate the Janus $\text{Mn}_2\text{Cl}_3\text{Br}_3$ for realizing high-temperature QAH effect. Therefore, the Janus $\text{Mn}_2\text{Cl}_3\text{Br}_3$ provide great promise for application in spintronic and electronic devices.

ACKNOWLEDGEMENTS

This work was carried out at Lvliang Cloud Computing Center of China, and the calculations were performed on TianHe-2.

-
- [1] K. v. Klitzing, G. Dorda, and M. Pepper, Phys. Rev. Lett. **45**, 494 (1980).
 - [2] D. J. Thouless, M. Kohmoto, M. P. Nightingale, and M. denNijs, Phys. Rev. Lett. **49**, 405 (1982).
 - [3] F. D. M. Haldane, Phys. Rev. Lett. **61**, 2015 (1988).
 - [4] C. X. Liu, S. C. Zhang and X. L. Qi, Annu. Rev. Condens. Matter Phys. **7**, 301 (2016).
 - [5] H. M. Weng, R. Yu, X. Hu, X. Dai and Z. Fang, Adv. Phys. **64**, 227 (2015).
 - [6] C. X. Liu, X. L. Qi, X. Dai, Z. Fang, and S. C. Zhang, Phys. Rev. Lett. **101**, 146802 (2008).
 - [7] R. Yu, W. Zhang, H. J. Zhang, S. C. Zhang, X. Dai and Z. Fang, Science **329**, 61 (2010).
 - [8] Z. H. Qiao, S. A. Yang, W. X. Feng, W. K. Tse, J. Ding, Y. G. Yao, J. Wang and Q. Niu, Phys. Rev. B **82**, 161414(R) (2010).
 - [9] J. Hu, J. Alicea, R. Wu, and M. Franz, Phys. Rev. Lett. **109**, 266801 (2012).
 - [10] H. Zhang, C. Lazo, S. Blugel, S. Heinze, and Y. Mokrousov, Phys. Rev. Lett. **108**, 056802 (2012).
 - [11] Z. H. Qiao, W. Ren, H. Chen, L. Bellaiche, Z. Y. Zhang, A. H. MacDonald and Q. Niu, Phys. Rev. Lett. **112**, 116404 (2014).
 - [12] M. Ezawa, Phys. Rev. Lett. **109**, 055502 (2012).
 - [13] H. Pan, Z. S. Li, C. C. Liu, G. B. Zhu, Z. H. Qiao, Y. G. Yao, Phys. Rev. Lett. **112**, 106802 (2014).
 - [14] T. P. Kaloni, N. Singh, and U. Schwingenschlogl, Phys. Rev. B **89**, 035409 (2015).
 - [15] P. Li, X. Li, W. Zhao, H. Chen, M. X. Chen, Z. X. Guo, J. Feng, X. G. Gong and A. H. MacDonald, Nano Lett. **17**, 6195 (2017).
 - [16] S. C. Wu, G. C. Shan, B. H. Yan, Phys. Rev. Lett. **113**, 256401 (2014).
 - [17] H. S. Zhang, T. Zhou, J. Y. Zhang, B. Zhao, Y. G. Yao, Z. Q. Yang, Phys. Rev. B **94**, 235409 (2016).
 - [18] D. Xiao, W. G. Zhu, Y. Ran, N. Nagaosa, and S. Okamoto, Nat. Commun. **2**, 596 (2011).
 - [19] T. Y. Cai, X. Li, F. Wang, S. Ju, J. Feng and C. D. Gong, Nano Lett. **15**, 6434 (2015).
 - [20] Y. L. Wang, Z. J. Wang, Z. Fang, and X. Dai, Phys. Rev. B **91**, 125139 (2015).
 - [21] Z. F. Wang, Z. Liu and F. Liu, Phys. Rev. Lett. **110**, 116801 (2013).
 - [22] L. Dong, Y. Kim, D. Er, A. M. Rappe, and V. B. Shenoy, Phys. Rev. Lett. **116**, 096601 (2016).
 - [23] X. M. Zhang, Z. H. Wang, M. W. Zhao, and F. Liu, Phys. Rev. B **93**, 165401 (2016).
 - [24] X. L. Sheng, and B. K. Nikolic, Phys. Rev. B **95**, 201402(R) (2017).
 - [25] C. X. Huang, J. Zhou, H. P. Wu, K. M. Deng, P. Jena, and E. J. Kan, Phys. Rev. B **95**, 045113 (2017).
 - [26] Q. L. Sun, and N. Kioussis, Phys. Rev. B **97**, 094408 (2018).
 - [27] P. Li, Phys. Chem. Chem. Phys. **21**, 6712 (2019).
 - [28] X. Y. Dong, J. F. Wang, R. X. Zhang, W. H. Duan, B. F. Zhu, J. O. Sofo and C. X. Liu, Nat. Commun. **6**, 8517 (2015).
 - [29] C. Z. Chang, J. Zhang, X. Feng, J. Shen, Z. Zhang, M. Guo, K. Li, Y. Ou, P. Wei, L. L. Wang, Z. Q. Ji, Y. Feng, S. Ji, X. Chen, J. Jia, X. Dai, Z. Fang, S. C. Zhang, K. He, Y. Wang, L. Lu, X. C. Ma and Q. K. Xue, Science **340**, 167 (2013).
 - [30] X. Kou, S. T. Gou, Y. Fan, L. Pan, M. Lang, Y. Jiang, Q. Shao, T. Nie, K. Murata, J. Tang, Y. Wang, L. He, T. K. Lee, W. L. Lee and K. L. Wang, Phys. Rev. Lett. **113**, 137201 (2014).
 - [31] C. Z. Chang, W. Zhao, D. Kim, Y. H. Zhang, B. A. Assaf, D. Heiman, S. C. Zhang, C. Liu, M. H. W. Chan and J. S. Moodera, Nat. Mater. **14**, 473 (2015).
 - [32] A. Y. Lu, H. Y. Zhu, J. Xiao, C. P. Chuu, Y. Han, M. H. Chiu, C. C. Cheng, C. W. Yang, K. H. Wei, Y. Yang, Y. Wang, D. Sokaras, D. Nordlund, P. Yang, D. A. Muller, M. Y. Chou, X. Zhang, and L. J. Li, Nat. Nanotechnol. **12**, 744 (2017).
 - [33] J. Zhang, S. Jia, I. Kholmanov, L. Dong, E. Er, W. Chen, H. Guo, Z. Jin, V. B. Shenoy, L. Shi, and J. Lou, ACS Nano **11**, 8192 (2017).
 - [34] G. Kresse and J. Hafner, Phys. Rev. B **47**, 558 (1993).
 - [35] G. Kresse and D. Joubert, Phys. Rev. B **59**, 1758 (1999).
 - [36] J. P. Perdew, K. Burke and M. Ernzerhof, Phys. Rev. Lett. **77**, 3865 (1996).
 - [37] S. L. Dudarev, G. A. Botton, S. Y. Savrasov, C. J. Humphreys, and A. P. Sutton, Phys. Rev. B **57**, 1505 (1998).
 - [38] F. Zhou, M. Cococcioni, C. A. Marianetti, D. Morgan, and G. Ceder, Phys. Rev. B **70**, 235121 (2014).
 - [39] Y. S. Hou, H. J. Xiang, and X. G. Gong, Phys. Rev. B **89**, 064415 (2014).
 - [40] A. Togo, F. Oba and I. Tanaka, Phys. Rev. B **78**, 134106 (2008).

- [41] N. Marzari and D. Vanderbilt, Phys. Rev. B **56**, 12847 (1997).
- [42] A. A. Mostofi, J. R. Yates, Y.-S. Lee, I. Souza, D. Vanderbilt and N. Marzari, Comput. Phys. Commun. **178**, 685 (2008).
- [43] M. P. L. Sancho, J. M. L. Sancho and J. Rubio, J. Phys. F **14**, 1205 (1984).
- [44] Q. S. Wu, S. N. Zhang, H.-F. Song, M. Troyer and A. A. Suluyanov, Comput. Phys. Commun. **224**, 405 (2018).
- [45] F. P. Li, W. Wei, P. Zhao, B. B. Huang, and Y. Dai, J. Phys. Chem. Lett. **8**, 5959 (2017).
- [46] G. Henkelman, A. Arnaldsson and H. Jónsson, Comput. Mater. Sci. **36**, 354 (2006).
- [47] N. D. Mermin, and H. Wangner, Phys. Rev. Lett. **17**, 1133 (1966).
- [48] W. B. Zhang, Q. Qu, P. Zhu and C. H. Lam, J. Mater. Chem. C **3**, 12457 (2013).
- [49] Y. Y. Deng, Y. J. Yu, Y. C. Song, J. Z. Zhang, N. Z. Wang, Z. Y. Sun, Y. F. Yi, Y. Z. Wu, S. W. Wu, J. Y. Zhu, J. Wang, X. H. Chen and Y. B. Zhang, Nature **563**, 94 (2018).
- [50] B. Huang, G. Clark, E. Navarro-Moratalla, D. R. Klein, R. Cheng, K. L. Seyler, D. Zhong, E. Schmidgall, M. A. McGuire, D. H. Cobden, W. Yao, D. Xiao, P. Jarillo-Herrero, and X. Xu, Nature **546**, 270 (2017).
- [51] Z. X. Guo, and A. Oshiyama, Phys. Rev. B **89**, 155418 (2014).
- [52] P. Li, J. X. Cao and Z. X. Guo, J. Mater. Chem. C **4**, 1736 (2016).
- [53] Z. X. Guo, S. Furuya, J. Iwata and A. Oshiyama, Phys. Rev. B **87**, 235435 (2013).
- [54] D. Xiao, M. C. Chang and Q. Niu, Rev. Mod. Phys. **82**, 1959 (2010).
- [55] X. Wang, J. Yates, I. Souza and D. Vanderbilt, Phys. Rev. B, **74**, 195118 (2006).
- [56] M. L. Sancho, J. L. Sancho, J. L. Sancho and J. Rubio, J. Phys. F **15**, 851 (1985).
- [57] I. Souza, N. Marzari and D. Vanderbilt, Phys. Rev. B **65**, 035109 (2001).
- [58] Y. Hatsugai, Phys. Rev. Lett. **71**, 3697 (1993).